



Contents lists available at ScienceDirect

Journal of Aerosol Science

journal homepage: www.elsevier.com/locate/jaerosci

Numerical simulation of welding fume lung dosimetry

Jianan Zhao^a, Yu Feng^{a,*}, Marcio Bezerra^b, Jun Wang^b, Ted Sperry^a

^a School of Chemical Engineering, Oklahoma State University, Stillwater, OK, USA

^b Department of Occupational and Environmental Health, College of Public Health, University of Oklahoma Health Sciences Center, Oklahoma City, OK, USA



ARTICLE INFO

Keywords:

Computational fluid-particle dynamics (CFPD)
Welding fume
Welding gas
Lung dosimetry

ABSTRACT

Exposures to airborne particles and toxic gases generated by welding fabrication activities will potentially lead to various diseases. Accurate information on the transport and deposition of such aerosols in the respiratory system is critically needed for precise health risk assessments. To address the data demand mentioned above, a multiscale computational fluid-particle dynamics (CFPD) model was developed in this study. Specifically, a virtual fabrication shop was integrated with a virtual human in the numerical model to evaluate the effects of ventilation condition, particle size, and gas species on the lung uptakes of those welding fume particles and gases. Welding fume particle and gases transmission, transport, and deposition have been simulated and analyzed starting from the emission source to the subject-specific human respiratory system via oral inhalation. Spherical iron particles with diameters of 100, 190, and 830 nm were simulated. The transport and absorption of NO_x and CO were predicted too. Steady-state inhalation with 11.87 L/min was applied with two different air filter ventilation conditions. The numerical results indicate that the ventilation condition can significantly influence welding gas transport and deposition. The pulmonary gas absorption rate is much higher at poor ventilation conditions. The air-tissue absorption coefficient is another crucial factor that can impact pulmonary gas absorption. The total particle deposition fractions (TDFs) from mouth/nose to generation 6 (G6) are less than 18.0%, and particles mostly deposit in the oral cavity. Regional and local particle deposition data demonstrate that particles tend to enter the two upper lobes more than the other three lobes. In summary, this study paves the way to build a personalized in silico tool based on CFPD models for noninvasive precise health risk assessments associated with different welding activities.

1. Introduction

Inhaling metal fume particles or gases generated by welding activities can cause serious health problems for workers. The particle size range is from approximately 100 nm to 800 nm (Wang, Hoang, Floyd, & Regens, 2017). Exposure to these aerosols poses severe health threats to workers as the toxic components can cause respiratory diseases, neurological ailments, and ultimately cancer (Hannu, Piipari, Tuppurainen, Nordman, & Tuomi, 2007; Sjögren, Hansen, Kjuus, & Persson, 1994). High-level exposures to welding fumes have been demonstrated to also cause acute systemic inflammation (Kim, Chen, Boyce, & Christiani, 2005). In addition, different gases are generated via vaporization and oxidization of the workpieces and the surrounding gases during the welding process (Golbabaie & Khadem, 2015). The most common toxic gases emitted are ozone (O₃), nitrous gases (NO_x), and carbon

* Corresponding author. School of Chemical Engineering, Oklahoma State University, 420 Engineering North, Stillwater, OK, 74078, USA.
E-mail address: yu.feng@okstate.edu (Y. Feng).

<https://doi.org/10.1016/j.jaerosci.2019.05.006>

Received 21 April 2019; Received in revised form 29 May 2019; Accepted 29 May 2019

Available online 03 June 2019

0021-8502/ © 2019 Elsevier Ltd. All rights reserved.

monoxide (CO) (Antonini, Taylor, Zimmer, & Roberts, 2004). Exposure to these gases can result in acute irritation, dizziness, and even lung damage. Specifically, research has shown that exposure to 0.16 ppm O₃ can cause irritation to human respiratory systems leading to shortness of breath, wheezing, and tightness in the chest (Horstman, Ball, Brown, Gerrity, & Folinsbee, 1995). High-level exposure to O₃ can lead to pulmonary edema (Scheel, Dobrogorski, Mountain, Svrbely, & Stokinger, 1959). Prolonged exposure to NO₂ may cause lung function disorders, such as reduced lung function and increased inflammation of the airways (Chitano, Hosselet, Mapp, & Fabbri, 1995; De Flora, 2000). NO_x has the potential to participate in many of the biological processes within the respiratory tract and to contribute to both the maintenance of normal homeostasis and to the disease pathogenesis of the disease (Al-Ali & Howarth, 1998). Besides the fatal risk caused by high-level CO exposure, acute low-level exposures to CO will also cause lung inflammation and reduce the function of different organs, resulting in impaired concentration, slow reflexes, and confusion (Kampa & Castanas, 2008). In addition, poor ventilation may result in higher concentrations of welding fume particles and gases in the workplace, which can increase exposure risk (Khadem et al., 2012).

The Occupational Safety and Health Administration (OSHA) does not currently have permissible exposure limits (PEL) for welding fume exposure. The current standard is based on the particulate matter measured in the breathing zone of the welders (NIOSH, 2019). However, the exposure level in the breathing zone is not the direct quantitative evidence of lung dosimetry. Specifically, higher exposure levels do not necessarily indicate higher lung uptakes and health risks. Hence, the exposure limits need to be "fine-tuned" based on the correlations between the exposure conditions and the resultant lung dosimetry data. Accordingly, the high-resolution data on how the metal particles and gases transport, deposit, and are absorbed in the human respiratory system is critically needed. Although there are various techniques for monitoring real-time experimental studies available that present transient exposure measurements for welders (Pires, Quintino, Amaral, & Rosado, 2010; Wang et al., 2017; Zhang et al., 2013), observations and measurements on regional and local lung deposition data from *in vitro* and *in vivo* studies are still very challenging due to the limitations of imaging resolution and operational flexibilities (Brand et al., 2013; Graczyk et al., 2016; Tian, Hindle, Lee, & Longest, 2015).

To overcome the drawbacks of the conventional investigating methods, high-fidelity computational fluid-particle dynamics (CFPD) models can be employed. The CFPD based models are capable of providing informative high-resolution deposition data based on the natural laws of physics in a noninvasive manner (Utzinger, 2004). In recent decades, several studies have been done on the development of CFPD models to predict the transport and deposition of particles and vapors in idealized and subject-specific human respiratory systems (Calmet et al., 2018; Feng & Kleinstreuer, 2014; Feng et al., 2018; Haghnegahdar, Feng, Chen, Lin, & Technology, 2018; Kim, Tong, Chan, & Yang, 2019; Kolanjiyil & Kleinstreuer, 2017; P. G. Koullapis, L. Nicolaou, & S. C. Kassinos, 2018; Lambert, O'Shaughnessy, Tawhai, Hoffman, & Lin, 2011; Longest et al., 2019; Xi et al., 2016; Xu, Shang, Tian, Weng, & Tu, 2018; Zhang, Kleinstreuer, & Hyun, 2012). Specifically, impressive research efforts have been made to predict lung dosimetry with simplified ambient conditions. Specifically, Xu et al. (2018) and Dong et al. (2018) constructed a hemispheric region around the virtual human face to mimic the realistic inspiratory airflows and particle distributions from the open space. The flow domains of ambient virtual environments were not reconstructed, and the transmissions of the particles from the generation sources to the human head regions were not simulated. Another great effort that has been done using a CFD model is to simulate the indoor fluid dynamics, i.e., distributions of airflow velocity, temperature, and contaminant concentration (Gupta, Lin, & Chen, 2012; Spengler & Chen, 2000). The resultant transport and deposition in human respiratory systems were not simulated. Recently, Yoo and Ito (2018) investigated the inhalation exposure of formaldehyde by applying hybrid physiologically-based pharmacokinetic (PBPK)-computational fluid dynamics (CFD) analyses to evaluate tissue dosimetry in respiratory tracts using an *in silico* human model. The study connected the indoor environment with a human airways model and investigated continuous vapor phase transport and absorption.

Although significant progress has been made on all the research mentioned above using CFPD based models, the inhalation boundary conditions are simplified, and the realistic exposure conditions were not employed for airborne discrete particulate matters. Therefore, a CFPD based multiscale modeling framework is developed in this paper to accurately simulate the transport phenomena of both discrete particulate matters and continuous gas phases from their indoor emission source to their transport endpoints in a subject-specific lung airway configuration. By simulating the welding fume particles with three diameters selected based on the field data (Wang et al., 2017) and four representative gas species (i.e., CO and NO_x) generated by welding fabrication processes, the local high-resolution transport, deposition, and absorption patterns in the indoor environment and human respiratory system were predicted. The extent of health effects was also analyzed based on the lung deposition data associated with two different ventilation conditions of the air filters. In particular, the multiscale CFPD model developed in this study is built on the well-validated Euler-Lagrange scheme (Feng et al., 2018), validated for the accuracy on simulating particle and gas transmission in a virtual fabrication shop, as well as the resultant transport and deposition in airways. To investigate the worst exposure scenarios, mouth breathing conditions were simulated rather than nose breathing conditions based on the fact that mouth breathers usually have higher lung depositions of inhaled particles (Haghnegahdar, Zhao, & Feng, 2019). With such a multiscale modeling framework, regional lung deposition and skin absorption can also be predicted based on different exposure conditions. It is worth mentioning that spherical shapes were assumed for the iron particles generated from mild steels with diameters 100, 190, and 830 nm. Parametric analysis was also performed to obtain insight on how the ventilation condition can impact the airway deposition and absorption of welding aerosols.

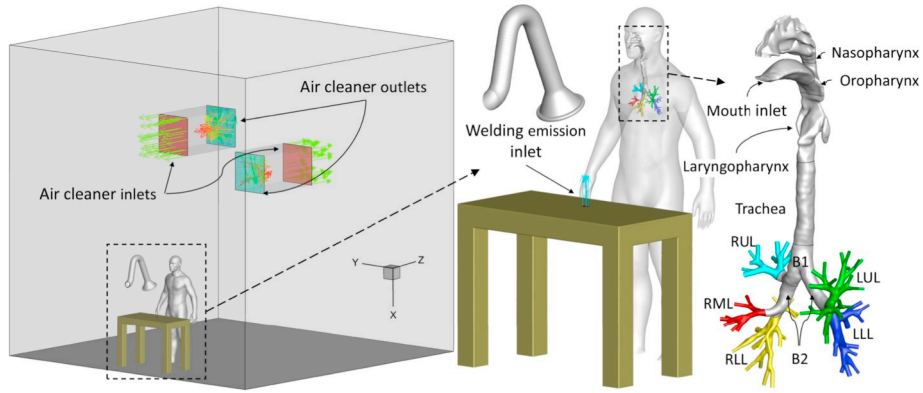


Fig. 1. Outline of the virtual indoor environment for welding and the virtual human system: (a) the virtual fabrication shop, (b) the detailed views of the virtual human, welding table, and the exhauster, and (c) the subject-specific human respiratory system.

2. Methods

2.1. Geometry

In order to accurately capture the impact of realistic indoor environments on welding aerosol emission and transmission, a multiscale flow domain is reconstructed for the numerical simulations using the validated CFPD model (Feng & Kleinstreuer, 2014; Feng, Kleinstreuer, Castro, & Rostami, 2016; Feng, Kleinstreuer, & Rostami, 2015; Feng et al., 2018; Haghnegahdar et al., 2019). Specifically, the geometry contains the virtual indoor welding environment and a virtual human with a subject-specific respiratory system connected at the mouth and nose with the body shell (see Figs. 1 (b) & (c)). Such a flow domain geometry enables the simulation of particle and gas transport from the emission site to the deposition sites, including the indoor surfaces, the human skin, and the human respiratory system. As shown in Fig. 1(a), the virtual fabrication shop with a dimension of $5\text{ m} \times 5\text{ m} \times 5\text{ m}$ was created with a welding table and an exhauster. Two rectangular ducts, representing Virtual Models of SS-2000 Free-Hanging Air Cleaners (Sentry Air System, Inc.), were built and positioned near the rooftop of the virtual fabrication shop (see Fig. 1(a) to mimic the realistic indoor ventilation conditions during the welding process. An emission source (0.04 m in diameter) was created on the table top as the generation source of welding fume particles and gases (see Fig. 1(b)). The coordinate of the emission source center is (0.0772, 0.0, -0.030) m, whereas the origin (0, 0, 0) of the geometry is at the front of the human nose (see Appendix A: Supplementary Data for additional details). The gravitational direction is aligned with the positive x -direction. The virtual human consists of a standing 47-year-old male body shell with a high-resolution human respiratory system covering the conducting zone from mouth/nose to generation 6 (G6). Lower generations were not included due to the limitations of imaging resolutions. The upper airways and tracheobronchial tree geometries are reconstructed from the computed tomography (CT) scans (Zhang et al., 2012). The virtual human body shell was reconstructed using Materialise Mimics and 3-matic to represent the welder in this numerical study. More details of the subject-specific respiratory system can be found in Fig. 1 (c) and previous experimental and numerical studies (Banko, Coletti, Schiavazzi, Elkins, & Eaton, 2015; Feng et al., 2018; Zhang et al., 2012).

2.2. Continuous phase

Considering the high computational cost using direct numerical simulation (DNS) and large eddy simulation (LES) (Cui & Gutheil, 2017; P. Koullapis, L. Nicolaou, & S. C. Kassinos, 2018; Nicolaou, 2018) to resolve the laminar-to-turbulence airflow field, the Transition Shear Stress Transport (SST) model (Menter, Langtry, & Völker, 2006) was employed to capture the characteristics of transitional airflow regime in the virtual fabrication shop and the human respiratory system. Early studies have confirmed the acceptable accuracy of the Transition SST model on the transitional airflow predictions compared with LES simulation results (Feng et al., 2018; Zhang & Kleinstreuer, 2011; Zhang, Kleinstreuer, & Feng, 2012). The continuity equation and Navier-Stokes equation for airflow can be given as:

$$\frac{\partial u_i}{\partial x_i} = 0 \quad (1)$$

$$\frac{\partial(\rho u_j u_i)}{\partial x_j} = -\frac{\partial p}{\partial x_i} + \frac{\partial}{\partial x_j} \left[(\mu + \mu_t) \left(\frac{\partial u_i}{\partial x_j} + \frac{\partial u_j}{\partial x_i} \right) \right] + \rho g_i \quad (2)$$

where u_i represents the averaged air velocity component in the i -direction, $g_i = (9.81, 0, 0)\text{ m/s}^2$ is the gravity, p is the pressure, and μ_t is the turbulent viscosity which can be given as:

$$\mu_t = \frac{\rho k f_\mu}{\omega} \quad (3)$$

In Eq. (3), k is the turbulence kinetic energy (TKE), f_μ is a function of strain rate magnitude, and ω is the specific rate of dissipation (Wilcox, 2006).

In addition, the energy transport equation employed in this study can be given as:

$$\frac{\partial T}{\partial t} + u_i \frac{\partial T}{\partial x_i} = \alpha \nabla^2 T + \frac{\nu \Phi_T}{c_p} \quad (4)$$

where T is the temperature, α is the thermal diffusivity, c_p represents the specific heat of the air at constant pressure, and $\nu \Phi_T$ stands for the rate of mechanical energy into internal energy per unit mass by viscous dissipation (Kleinstreuer, 1997).

During the welding process, multiple gas species are produced, which are harmful to humans via skin absorption and oral/nasal inhalations. In this study, four gases (N_2O , NO , NO_2 , and CO) were simulated and governed by the species transport equation with turbulence dispersion:

$$\frac{\partial(\rho_{a-g} u_j Y_s)}{\partial x_j} = \frac{\partial}{\partial x_j} \left[\left(\rho_{a-g} \tilde{D}_{a-g,s} + \frac{\mu_t}{\sigma_Y} \right) \frac{\partial Y_s}{\partial x_j} \right] \quad (5)$$

where Y_s is the mass fraction of the s -th gas species ($s=1, 2, 3, \text{ or } 4$), $\sigma_Y=0.9$ is the turbulent Schmidt number (Feng et al., 2016), ρ_{a-g} is the mixture density, and $\tilde{D}_{a-g,s}$ is the molecular diffusivity of the s -th gas species in the air, which can be modeled by:

$$\tilde{D}_{a-g,s} = D_{a-g,s}(0,1) \left(\frac{P_0}{P} \right) \left(\frac{T}{T_0} \right)^{1.81} \quad (6)$$

where $D_{a-g,s}(0,1)$ is the molecular diffusivity of s -th gas in air at standard temperature and pressure (STP). Specifically, the standard temperature T_0 is equal to 0°C , which is 273.15 K, and the standard pressure P_0 is equal to 1 atm (101.3 kPa). The values of $D_{a-g,s}(0,1)$ (Massman, 1998) are listed in Table 1.

Gases are assumed to be nonreactive to each other during the transport and absorption processes. Gas concentrations at both sides of the air-mucus interface are assumed in equilibrium and always satisfy Henry's law. Due to the rapid removal of gas molecules through the tissue, gas concentrations in the tissue $Y_{s,i}$ are assumed to constantly equal to zero (Feng et al., 2016). The 3rd-type boundary condition is employed at airway walls for gas absorption:

$$\left. \frac{\partial Y_s}{\partial n} \right|_w = \frac{Y_{s,c} - Y_{s,w}}{0.5 h_{cell}} = \Gamma_{s,w} \cdot Y_{s,w} \quad (7)$$

where $Y_{s,c}$ is the mass fraction at the center of the near-wall mesh cell, $Y_{s,w}$ is the mass fraction at the mesh wall surface, $\Gamma_{s,w}$ is the airway wall absorption coefficient (Feng et al., 2016), and h_{cell} is the height of the near-wall prism layer. Accordingly, the overall absorption mass flow rate can be expressed as:

$$\dot{m}_{s,wall} = \sum_{i=1}^n j_{s,i} S_i \quad (8)$$

Here, S_i is the wall surface area of the i -th cell and $j_{s,i}$ is the wall mass flux of s -th species at the i -th wall surface cell, which can be calculated as

$$j_{s,i} = \left(\rho_{a-g} \tilde{D}_{a-g,s} + \frac{\mu_t}{\sigma_Y} \right) \Gamma_{s,w} \cdot Y_{s,i} \Big|_w \quad (9)$$

where $Y_{s,i} \Big|_w$ is the s -th gas mass fraction in the i -th wall surface cell.

To evaluate the regional gas uptake, the absorption fraction (AF) of the continuous phase can be defined as:

$$\text{AF}_s = \frac{\dot{m}_{s,wall}}{\dot{m}_{s,total}} \quad (10)$$

where $\dot{m}_{s,total}$ is the s -th gas mass flow rate via oral inhalation.

Table 1

Physical properties of selected gases including relative molecular mass M_s , coefficients of diffusivity $D_{a-g,s}$ in the air at STP (Massman, 1998) and, $D_{a-w,s}$ in water at 310.15 K (Poudyal & Adhikari, 2014; Tamimi, B. Rinker, & Sandall, 1994; Zacharia & Deen, 2005), dimensionless gas-liquid partition equilibrium coefficient $k_{H,s}$ (Sander, 2015), and airway wall absorption coefficient $\Gamma_{s,w}$.

Gas	M_s	$D_{a-g,s}(0,1)$	$D_{a-w,s}$	$k_{H,s}$	$\Gamma_{s,w}$
N_2O	44	0.1436	2.43	2.40×10^{-4}	7.06×10^4
NO	30	0.1802	2.21	1.90×10^{-5}	6.45×10^5
NO_2	46	0.1361	1.86	1.20×10^{-4}	1.14×10^5
CO	28	0.1807	3.26	9.70×10^{-6}	1.86×10^6

2.3. Particle phase

The one-way coupled Euler-Lagrange approach was applied to predict the trajectories of each particle generated by the welding processes (Feng et al., 2018). Particles were assumed to be spherical and solid with constant particle diameters, which were emitted from the top of the welding table (see Fig. 1). In this study, particle-particle interactions and the thermophoretic motion were neglected by adopting the dilute particle suspension assumption. The translational motion of each particle is governed by the force balance equation, i.e., Newton's second law. To determine the particle velocity u_i^P , and position x_i^P , the force balance equation for each particle can be given by:

$$\frac{dx_i^P}{dt} = u_i^P \quad (11)$$

$$m_p \frac{d}{dt}(u_i^P) = F_i^D + F_i^L + F_i^{BM} + F_i^G + F_i^T \quad (12)$$

Here, m_p is the particle mass, F_i^D represents the drag force (Chen, Feng, Zhong, & Kleinstreuer, 2017), F_i^G is the gravitational force, F_i^{BM} is the Brownian motion induced force (Feng et al., 2016; Li & Ahmadi, 1993), F_i^T is the fluctuating force due to turbulence (Gosman & Ioannides, 1983), and F_i^L is the Saffman lift force (Saffman, 1965). Particles are considered as deposited, if the distance between the particle center and the airway wall is equal to or less than the particle radius. More details of all forces in Eq. (12) can be found in previous studies (Feng et al., 2018). Specifically, particles are assumed to be spherical and the density is $7,870 \text{ kg/m}^3$, since the majority of particles is iron based on the in-house measurements (Wang et al., 2017).

Similar to Eq. (10), the regional deposition of particles in human airways can be quantified by either the regional deposition fraction $DF_{\text{mouth}}(\text{region})$ or the regional deposition efficiency $DE(\text{region})$ which are defined as (Feng et al., 2018):

$$DE(\text{region}) = \frac{\text{Number of deposited particles in a specific region}}{\text{Number of particles entering this region}} \quad (13)$$

$$DF_{\text{mouth}}(\text{region}) = \frac{\text{Number of deposited particles in a specific region}}{\text{Number of particles entering the mouth}} \quad (14)$$

To provide physical insight for the particle transport and deposition in the virtual welding fabrication room, the regional deposition fraction of fume particles based on the particles emitted at the table top, $DF_{\text{em}}(\text{region})$ is defined as:

$$DF_{\text{em}}(\text{region}) = \frac{\text{Number of deposited particles in a specific region}}{\text{Number of particles released at welding source}} \quad (15)$$

Combined with the experimental data (Wang et al., 2017b), the evaluation of DF_{em} can be used to estimate the realistic number of deposited particles in each sub-region of the airway during the welding process (see Future Work and Appendix A: Supplementary Data for more details).

3. Numerical model

3.1. Poly-hexcore mesh generation and independence test

Computational meshes were generated using ANSYS Fluent Meshing 19.2 (ANSYS Inc., Canonsburg, PA). Considering the complexity of the flow domains with the virtual welding fabrication shop, the virtual human body shell, and the subject-specific human respiratory system in this study, the poly-hexcore meshing feature was employed. Specifically, the mosaic technology for the poly-hexcore mesh generation was used to fill the bulk region with octree-based hexahedrons and the near-wall boundary layer with poly-prisms, and conformally connect the two meshes with general polyhedrons (see Fig. 2). Compared with the conventional unstructured tetrahedral mesh, the poly-hexcore mesh has fewer and better-quality mesh elements, requiring less memory, and delivered a solution approximately two-times faster with higher accuracy. In this study, six near-wall prism layers were generated to resolve the boundary layer flow patterns accurately. The mesh topology was determined by refining the mesh until mesh independence of the flow field solutions was achieved. The details of the three computational meshes used to perform the independence test are listed in Table 2. Velocity profile comparisons for the mesh independence test are documented in Appendix A: Supplementary Data. The final mesh (Mesh 2 in Table 2) contains approximately 19.6 million cells and 43.9 million nodes. The mesh cells in the nasal cavity, oropharynx, and laryngopharynx were refined to guarantee that the thickness of the first prism layer satisfies $y^+ < 1$, where y^+ is the dimensionless wall distance (Menter et al., 2006; Menter, 1994). The maximum skewness of the final mesh elements is below 0.8, with a maximum aspect ratio of 30.7.

3.2. Numerical setup

The governing equations with appropriate initial and boundary conditions were solved using a finite-volume based commercial program, i.e., ANSYS Fluent 19.2 (ANSYS Inc., Canonsburg, PA). In-house user-defined functions (UDFs) were developed and employed for: (1) Simulating the gas species transport and absorption, (2) Recovering the near-wall anisotropic turbulence fluctuation velocities (Bernate, Geisler, Padhy, Shaqfeh, & Iaccarino, 2017), (3) Modeling Brownian motion induced fluctuation velocities of

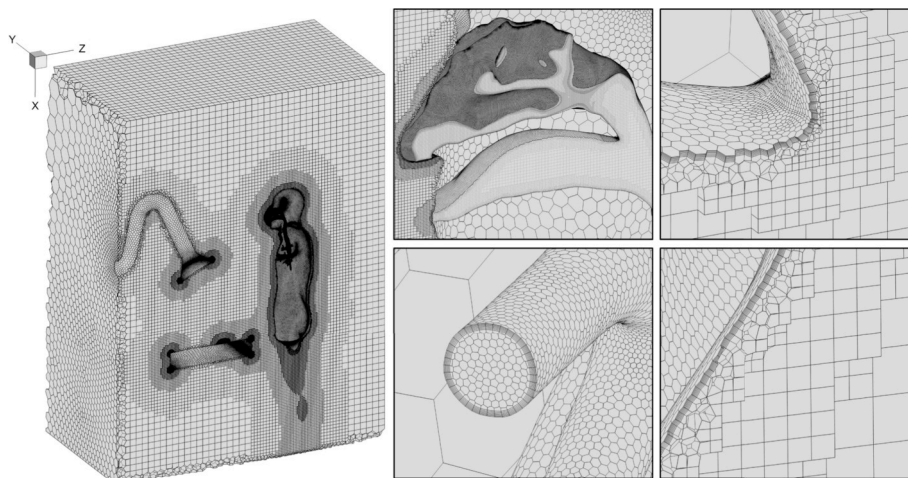


Fig. 2. Details of the final poly-hexcore mesh (Mesh 2) for the virtual welding fabrication shop and virtual human.

Table 2

Details of the meshes generated for the independence test.

Mesh	Mesh cell numbers in each region ($\times 10^6$)		
	Room	Airways	Total
Mesh 1	5.6	4.8	10.4
Mesh 2 (Final)	8.0	11.6	19.6
Mesh 3	14.5	20.7	35.2

particles (Feng et al., 2018; Mansour & Rhee Xiao Wu, 2009), and (4) Post-processing particle deposition and gas absorption data in human respiratory systems. Numerical simulations were performed on a local Dell Precision T7810 workstation (Intel® Xeon® Processor E5-2643 v4 with two processors, 64 cores and 128 GB RAM).

This study examined both 1,000 and 2,000 CFM (0.472 and 0.944 m³/s) at the air filter inlets ($V_{out,Af} = 1.27$ and 2.54 m/s, respectively) and enforced a zero pressure surface to solve the room exhaust velocity out of the air filter outlets (see Fig. 1(a)). Based on flow settings and welding gun nozzle size, the shielding gas flow rate ranges from 10 to 100 CFH (4.72–47.2 L/min) (Hou, Evans, McClure, Nunes, & Garcia, 1996). This study adopted a flow rate equal to 30 CFH (14.16 L/min) (WAT, 2019). Accordingly, the gas mixture velocity emitted at the table top was set to $V_{mix,em} = 0.874$ m/s. Steady-state inspiratory flows were assumed. The mass flow rates at the airway outlets of the five lobes are listed in Table 3, which were acquired from the open literature (Sul et al., 2018). The equivalent average volumetric inhalation flow rate was equal to 11.87 L/min, representing the breath at rest (Daigle et al., 2003; Heyder, 2004). The elliptical mouth opening was reconstructed with a hydraulic diameter of approximately 9.5 mm as the airway inlet.

For the temperature boundary conditions, an average temperature of 1,100 K was assigned to the metal fume emission inlet on the table top (Goldak, Chakravarti, & Bibby, 1984). The human body temperature was assumed to be 310 K, and the ambient temperature was set to 296 K.

To quantify emitted gas species distribution and absorption on a different scale to a notionally common scale, the normalized mass fraction of gas species is defined as:

$$\tilde{Y}_s = \frac{Y_s}{Y_{s,em}} \quad (16)$$

Table 3

Outlet boundary conditions with realistic mass flow rate distributions among 5 lobes.

Lung Lobe Outlet	Volumetric Flow Percentage (%) (Sul et al., 2018)	Volumetric Flow Rate (L/min)	Equivalent Air Flow Rate (kg/s)
Right Upper Lobe (RUL)	21.67	2.57	5.25×10^{-5}
Right Middle Lobe (RML)	11.11	1.32	2.69×10^{-5}
Right Lower Lobe (RLL)	19.44	2.31	4.71×10^{-5}
Left Upper Lobe (LUL)	25.56	3.03	6.20×10^{-5}
Left Lower Lobe (LLL)	22.22	2.64	5.39×10^{-5}
Total	100	11.87	2.42×10^{-4}

where $Y_{s,em}$ is the mass fraction of s -th gas at the welding emission inlet. Accordingly, $\bar{Y}_{s,em}$ (\bar{Y}_s at the emission source) were all equal to 1.0. The gas species mass fraction at the air filter inlets was set to zero indicating 100% toxic gas absorption by air filters. The 3rd-type boundary condition (see Eq. (7)) was applied to the airway walls for the accurate evaluation of the near-wall mass fractions and gas absorption rates, while non-absorption boundary conditions were set to all other walls. Based on Eq. (9), absorption mass flux based on the normalized mass fraction (\bar{Y}_s) are denoted as \bar{j}_s .

Due to the high particle number concentration of metal fumes at the welding emission source (i.e., particle number emission rate is from 10^8 to 10^{10} particles/s) (Wang et al., 2017), the computational cost using the Lagrange tracking scheme was unaffordable. Therefore, a two-step scale-up method of the particle number was employed and described as follows:

- (1) Scaled indoor simulation for predicting DF_{em} on the human body and the inhaled fraction at the mouth opening. To reduce the computational time and maintain the prediction accuracy, a reduced number of particles were injected and simulated. Specifically, in the steady-state flow field, the ratio between the number of particles inhaled by the virtual human or deposited on human body and the number of particles emitted should be a constant after the total number of particles emitted in a unit time is larger than a specific value, which is defined as the critical particle number N_{cr} . Thus, the particle-number independence tests were performed (see Fig. S2 in Appendix A: Supplementary Data), and $N_{cr} = 33,990$ were determined. With 33,990 particles entered into the flow domain at the welding emission source, the inhaled fraction at the mouth opening $DF_{em}(\text{mouth})$ was simulated and quantified, which can represent the fractions that can be obtained with the real number of particles emitted. All the particles were injected at the welding emission source (see Fig. 1(b)) with an initial velocity $V_{p,em} = 6.8$ m/s and an injection angle of 60° relative to the table top. –The random particle initial distributions were generated using an in-house MATLAB code. Particle time step sizes for different diameters (100, 190, and 830 nm) (Wang et al., 2017) are 2.77×10^{-6} , 5.68×10^{-6} , and 3.78×10^{-5} s, respectively (Feng et al., 2018). The simulation was considered completed at 130 s, when more than 95% of the particle tracking had been completed.
- (2) Prediction of the transport and deposition of inhaled particles. With a separate particle number independence test, 10^5 particles were released at the mouth inlet with an initial velocity of 2.2 m/s (i.e., mouth inlet area-weighted average velocity) along the z -axis. Three sizes of particles (100, 190, and 830 nm) (Wang et al., 2017) were investigated. The particle transport simulation reached completion as the fraction of incomplete particles (neither deposit nor escape through lobe outlets at G6) was less than 5% of total inhaled particles.

4. Results and discussion

4.1. Model validations

The CFPD model employed in this study has been well validated in previous studies with benchmark experimental data (Feng et al., 2015; Feng, Zhao, Chen, & Lin, 2017; Feng et al., 2018; Y. Feng & C. Kleinstreuer, 2013; Haghnegahdar et al., 2018; Zhang et al., 2012). Specifically, model validations have been done for both the primary and secondary phases.

- (1) *Primary Phase.* For the airflow field prediction, the Transition SST model has been affirmed as an accurate and time-saving Reynolds-averaged Navier-Stokes (RANS) model to simulate laminar-to-turbulence transitional airflow regime (Banko et al., 2015; Feng et al., 2017). The model has been extensively validated with benchmark experimental data (Banko et al., 2015) in the same subject-specific respiratory system used in this study (Feng et al., 2017). Good agreements between our numerical simulations and two independent experiments and numerical studies were observed, indicating the reliability of the CFPD modeling framework.
- (2) *Secondary Phase.* For particle transport dynamics, the Lagrange model for discrete phase transport and deposition in subject-specific human respiratory systems has been validated in previous publications (Chen et al., 2017; Feng & C. Kleinstreuer, 2013; Feng & Kleinstreuer, 2014; Feng et al., 2015; Feng et al., 2018).

4.2. Airflow velocity and temperature fields

Fig. 3 (a) shows the steady-state temperature distribution near the virtual human in the indoor environment. The heat dissipation rate is high above the welding emission source due to the high-temperature gradient between the emission source and the ambient room environment. In contrast, the temperature distribution in the respiratory tract is significantly affected by convection. For example, the oral inhalation impingement jet and laryngeal jet shown in Fig. 4 (a) indicate strong forced convections, which introduce the low-temperature airflow stream from the ambient air and cause the local uneven temperature distributions (see Fig. 4 (b)).

Fig. 3 (b) illustrates the airflow field distribution in the virtual fabrication shop colored by the velocity magnitude $\|\vec{V}\|$. Two ventilation free jets are developed near the air filter outlets. As the jets impact the wall, impingements are formed. The airflow velocities decrease to zero at the jet core regions when the jets strike the walls, while the outer regions are redirected along the wall surfaces and form the wall jets. The redirected flow near the room ceiling forms a vortex and a recirculation zone (see Fig. S3 in Appendix A: Supplementary Data).

Furthermore, Figs. 4 (a) and (b) visualize the velocity magnitude distribution in the airways at the sagittal plane ($y = -7.5$ mm)

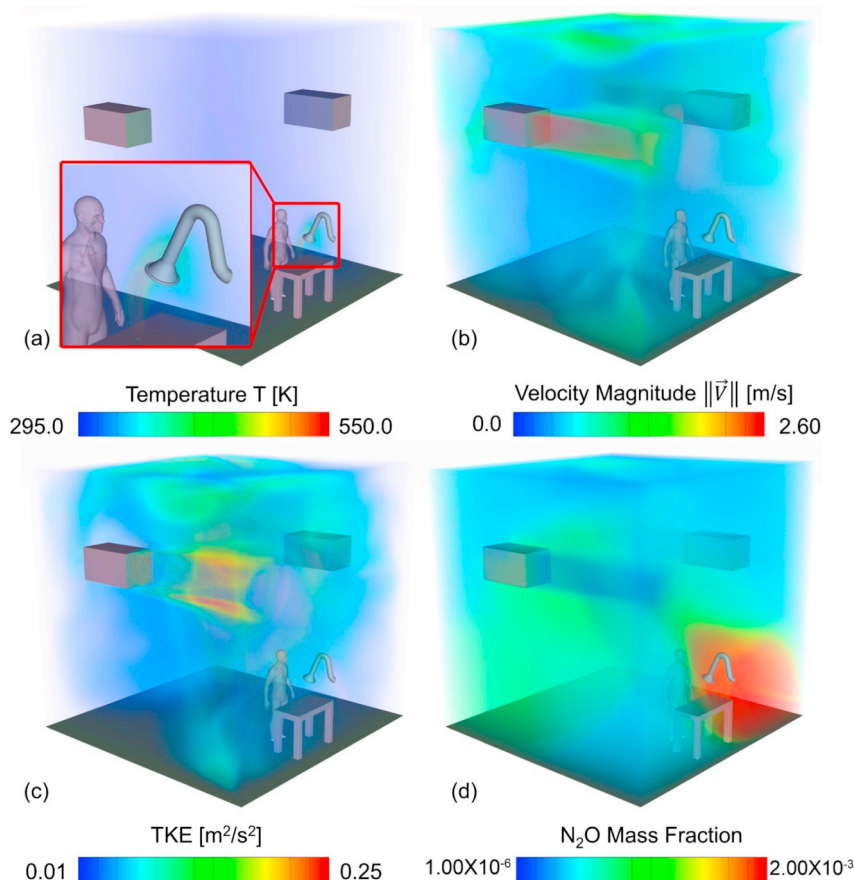


Fig. 3. Visualizations of the N₂O transport phenomena in the virtual fabrication shop: (a) temperature, (b) velocity magnitude, (c) TKE, and (d) N₂O mass fraction.

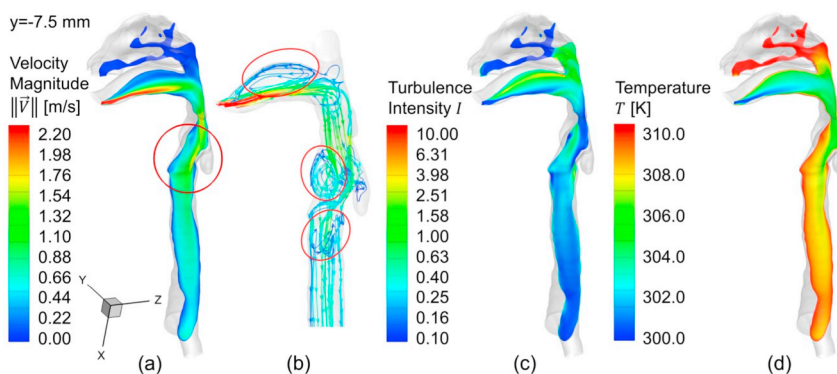


Fig. 4. Scalar distributions at the sagittal plane ($y = -7.5 \text{ mm}$) in airway model: (a) velocity magnitude $\|\vec{v}\|$, (b) streamlines colored by velocity magnitude, (c) turbulence intensity I , and (d) temperature T .

and the streamlines in the upper airway, respectively. Three main recirculation zones are formed in the upper airway (see the red circles in Fig. 4 (b)), which are critical to the toxic gases transport and absorption in the respiratory tract. As the airflow enters the mouth, an oral inhalation impingement jet is formed. A recirculation zone is generated near the upper palate due to the abrupt cross-section expansion in the oral cavity. The second recirculation zone occurs below the epiglottis which is also due to the airflow passage expansion. The laryngeal jet at glottis that can be observed in Fig. 4 (a), leads to the flow recirculation in laryngopharynx. The recirculation dissipates quickly as the flow moves further downstream to the trachea.

High TKE can be found near the ceiling of the virtual welding fabrication shop, where recirculations and vortices are developed (see Fig. 3 (c)). Fig. 4 (c) shows the distribution of the turbulence intensity I (Lin, Tawhai, McLennan, & Hoffman, 2007) in the lung at

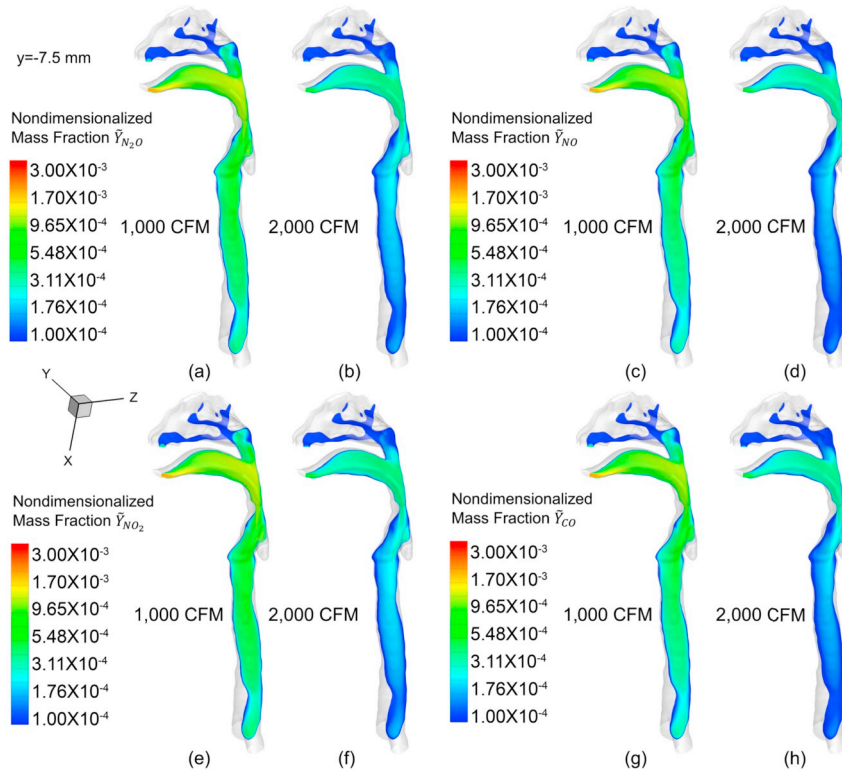


Fig. 5. Normalized mass fraction distributions of different gases at the sagittal plane ($y = -7.5$ mm) of the human respiratory system with different ventilation conditions: (a) N_2O at 1,000 CFM, (b) N_2O at 2,000 CFM, (c) NO at 1,000 CFM, (d) NO at 2,000 CFM, (e) NO_2 at 1,000 CFM, (f) NO_2 at 2,000 CFM, (g) CO at 1,000 CFM, and (h) CO at 2,000 CFM.

the sagittal plane ($y = -7.5$ mm). High turbulence intensity can be found in the oral cavity near the upper palate and laryngopharynx due to the regional recirculation. In contrast, the high turbulence intensity in the nasopharynx is because of the low mean velocity magnitude in this region for the mouth breathing scenarios simulated in this study.

4.3. Welding gases transport and absorption

Fig. 3 (d) shows the distribution of the normalized N_2O mass fraction, \bar{Y}_{N_2O} , in the virtual fabrication shop. Near the emission source, the high temperature plays a vital role in species transport (see Fig. S4 in Appendix A: Supplementary Data) as $\bar{D}_{a-g,s}$ varies proportionally to $T^{1.81}$. As the temperature decreases, species transport is significantly affected by airflow convection. Supported by the additional details provided in Figs. S3 (b) and Fig. S6 in Appendix A: Supplementary Data, emitted gases transport along the airflow streamlines to the left of the virtual human, bringing the high-concentration N_2O directly from the emission source to the left corner without being filtered (see Fig. 3 (d)). After entering the recirculation zone (i.e., dead zone) located and restricted in the left corner of the room, gas diffusion becomes relatively more important. As a result, the uniform distribution of \bar{Y}_{N_2O} is developed in this region with weak forced convection (see the low $\|V\|$ in this region shown in Fig. S3 (b) in Appendix A: Supplementary Data, as well as the low $\|\bar{V}_{mix,em}\|$). On the contrary, N_2O concentration is low in the ventilation jet generated by the air filters due to the filtration effects. N_2O concentration is relatively high near the room ceiling, which is because of the direct gas transport from the emission source to this region without passing the air filters (also see the streamlines shown in Figs. S3 (b) and (c) in Appendix A: Supplementary Data). Therefore, results shown in Fig. 3 (d) indicate the importance of the ventilation design, in order to avoid the formation of “dead zones” with high concentrations of toxic gas in the indoor environment.

Fig. 5 illustrates the steady-state gas distributions in the respiratory tract at the sagittal plane ($y = -7.5$ mm). As shown in Figs. 5 (a), (c), (e), and (g), \bar{Y}_s distributions are different among gases, which is mainly because of the difference in their diffusivities ($\bar{D}_{a-g,s}$). Indeed, $\bar{D}_{a-g,s}$ decreases with the reduction of the relative molecular mass. The strong flow convection in the oral cavity and the mixing effect of the recirculation region at the upper palate result in more uniform distribution of \bar{Y}_s and their relatively high near-wall gradients. After gases pass the glottis, for cases with a ventilation rate of 2,000 CFM, the gas absorption effect on \bar{Y}_s distribution is prominent in the near-wall region. Specifically, since the absorption rate of NO is higher at the wall than N_2O (see Fig. 6 (a) and (c)), \bar{Y}_{NO} is lower than \bar{Y}_{N_2O} near the wall (shown in Fig. 5 (a) and (c)). The nonzero \bar{Y}_s is observed in the nasopharynx and nasal cavity, which is due to the diffusion driven by the local concentration gradient.

As an example, Fig. 6 compares the local absorption mass flux distributions of N_2O and NO , i.e., $\bar{j}_{N_2O,wall}$ and $\bar{j}_{NO,wall}$, with different

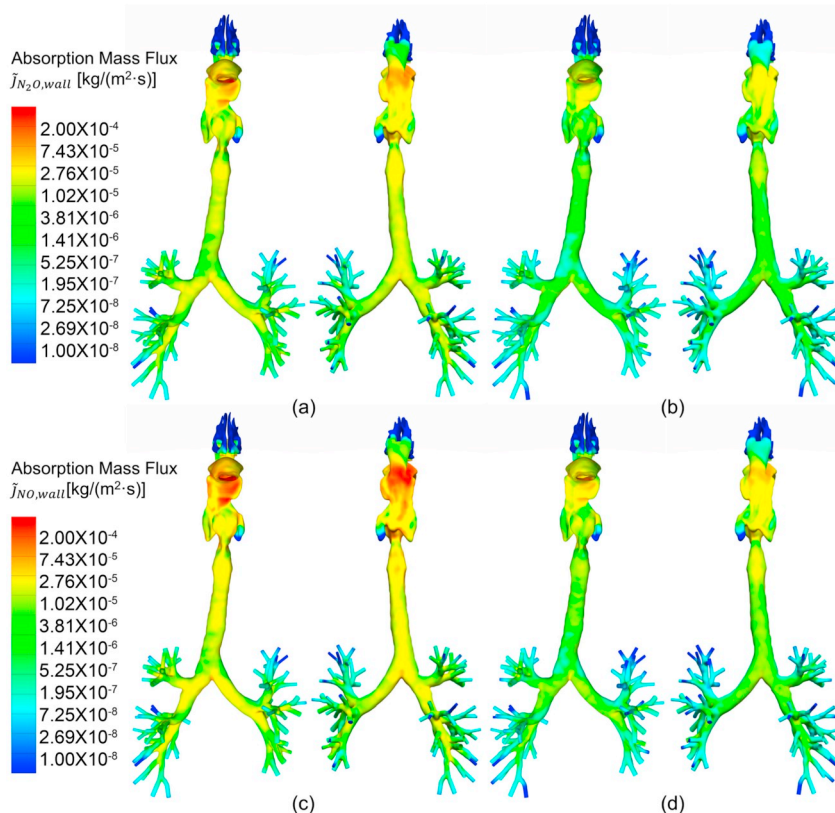


Fig. 6. Absorption mass flux distributions of the inhaled N_2O and NO in the subject-specific human respiratory system: (a) N_2O at 1,000 CFM, (b) N_2O at 2,000 CFM, (c) NO at 1,000 CFM, and (d) NO at 2,000 CFM.

ventilation conditions (additional comparisons of NO_2 and CO are shown in Fig. S8 in Appendix A: Supplementary Data). The distributions of $\bar{j}_{s,wall}$ in the nasopharynx and the nasal cavity are driven by the localized dominant diffusion since the inhalation flow rates are equal to zero at both nostrils for the mouth breathing scenarios simulated in this study. $\bar{j}_{s,wall}$ distributions in the oral cavity and oropharynx are induced by the secondary flow of the recirculation and the inhalation impingement jet. The asymmetrical distribution of $\bar{j}_{s,wall}$ at left and right sides in the laryngopharynx is due to the asymmetrical airflow distribution shown in Fig. 4 (b). Another high concentration region of $\bar{j}_{s,wall}$ is near the upper back trachea. This high-concentration region is because of the direct laryngeal jet impaction circled in Fig. 4 (a), which carries the high-concentration gases to the near-wall region. In the tracheo-bronchial tree, high $\bar{j}_{s,wall}$ can be observed near the carina and other bifurcating points that resulted from the direct impaction. The relatively high $\bar{j}_{s,wall}$ is observed in the oral cavity where the AFs of N_2O and NO are 21.4% and 37.0% at 2,000 CFM as shown in Fig. 7, respectively.

Fig. 7 displays the regional AFs of selected gases under different ventilation conditions. To provide maximum estimations of the gas absorption, it was assumed that gases reach the truncated G6 airway outlets can be all absorbed by the lower airways. Simulation results show that at 2,000 CFM, the total AFs of N_2O and NO are 51.2% and 90.1%. The total AF of NO is higher because of its relatively higher solubility. At 1,000 CFM, similar trends can be observed, i.e., the total AFs of N_2O and NO in airways are 51.0% and 90.1%, respectively. Compared with the percentages of the gases entering the mouth, over 37.0% of NO and CO as well as approximately 22.0% of N_2O and NO_2 are absorbed in the oral cavity. Furthermore, approximately 80% of NO and CO , as well as 46% of N_2O and NO_2 , are absorbed in the upper airway. Based on the total AFs obtained from the simulation results, the assumption of 100% gas absorption by the airways (Spengler & Chen, 2000) is not accurate. With the nonreactive gas assumption, the large differences among total AFs are determined by the airway wall absorption coefficient $\Gamma_{s,w}$ (see Eq. (7)). From the perspective of total absorbed gases at 2,000 CFM for the ventilation condition, the amounts of absorbed gases (N_2O , NO , NO_2 and CO) are on the same level in the upper airway (from mouth/nose to the trachea), which account for 81.6%, 86.3%, 81.2% and 86.6% of the total absorptions, respectively.

4.4. Welding fume particle transport and deposition

Fig. 8 depicts the local particle deposition patterns in the human respiratory system. The “hot spots” of particle deposition are the front and back sides of the oropharynx. Such concentrated particle deposition patterns are induced by the direct particle impactions either carried by the inhalation impingement jet or the reflected high-velocity stream. For the mouth breathing without forced convections in the nose, there is still a small portion of the inhaled particles trapped in the nasal cavity driven by the diffusion effect

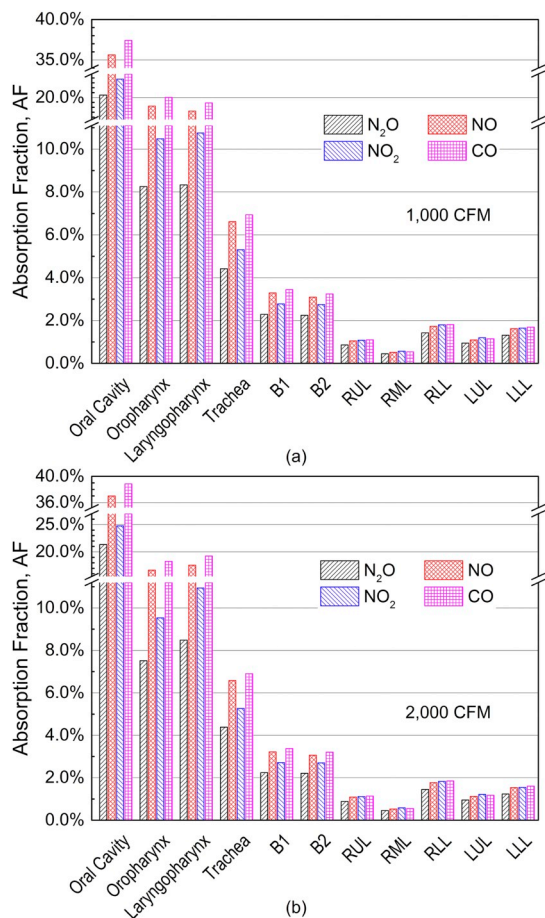


Fig. 7. Regional gas absorption fractions (AFs) in the human respiratory system with two ventilation conditions: (a) 1,000 CFM and (b) 2,000 CFM.

(see Fig. 8 (a)-(c)). The inertial impaction on particle deposition is more evident for more massive particles ($d_p = 830$ nm), based on the more concentrated deposition patterns shown in Fig. 8 (c) than the distributed depositions of smaller particles ($d_p = 100$ nm and 190 nm) shown in Fig. 8 (a) and (b). The particle deposition patterns in the oral cavity are a combined consequence of particle size induced inertial impaction, Brownian motion, and gravitational sedimentation. Microparticles tend to follow the flow pattern well, so that they transport along the streamlines in the recirculation region in the oral cavity (also see Fig. 4 (b)). Compared with the larger particles ($d_p = 830$ nm), depositions of smaller particles ($d_p = 100$ nm and 190 nm) in the oral cavity are more uniformly distributed, since smaller particles have stronger Brownian motion than large particles. The deposition pattern of larger particles ($d_p = 830$ nm) is more concentrated, especially at the lower palate in the oral cavity. Such deposition patterns are because of the more dominant gravitational sedimentation and inertial impaction effects. Another mechanism leading to depositions is the interception, which can be qualitatively visualized by the TKE or turbulence intensity (I). In the oral cavity, I is relatively high near the upper palate, while low near the lower palate (see Fig. 4 (c)). Smaller particles ($d_p = 100$ nm) that deposit at the back of the oropharynx with the residence time less than 0.1 s are because of the direct impaction. Compared with smaller particles, fewer larger particles are trapped at the back oropharynx and larynx. Instead, the deposition concentrates at the front oropharynx due to the gravitational effects, which leads to slightly higher $DF_{\text{mouth}}(\text{oropharynx})$ than 190 nm particles (see Fig. 9 (b)).

The laryngeal jet and its related recirculation zone have significant impacts on particle deposition patterns, especially for particles that deposit at the laryngopharynx and upper trachea. Particle deposit at the lower trachea is mainly due to the Brownian motion or interception, since the particle residence times are generally longer than 1.0 s. In addition, concentrated deposition can be observed at bifurcating points in the tracheobronchial tree, which are mainly due to the inertial impaction and gravitational sedimentations (see Figs. 8 (a)-(c)).

Figs. 9 (a) and (b) display the RDEs and the RDF_{mouths} . Total deposition fractions TDF_{mouth} are 16.7% (for 100 nm), 14.8% (for 190 nm), and 17.3% (for 830 nm), indicating more than 80% of the particles can penetrate into small airways. The higher TDF_{mouth} for $d_p = 830$ nm is mainly because of the dominantly higher $DF_{\text{mouth}}(\text{oral cavity})$ compared with 100 nm and 190 nm particles. Except for the oral cavity, oropharynx, and B2, RDF_{mouth} 's decrease as the particles become larger. The non-monotonic trend of RDF_{mouth} against particle size in the oropharynx and B2 are due to the combined effects of multiple deposition mechanisms, i.e., inertial impaction, gravitational sedimentation, interception, and Brownian motion.

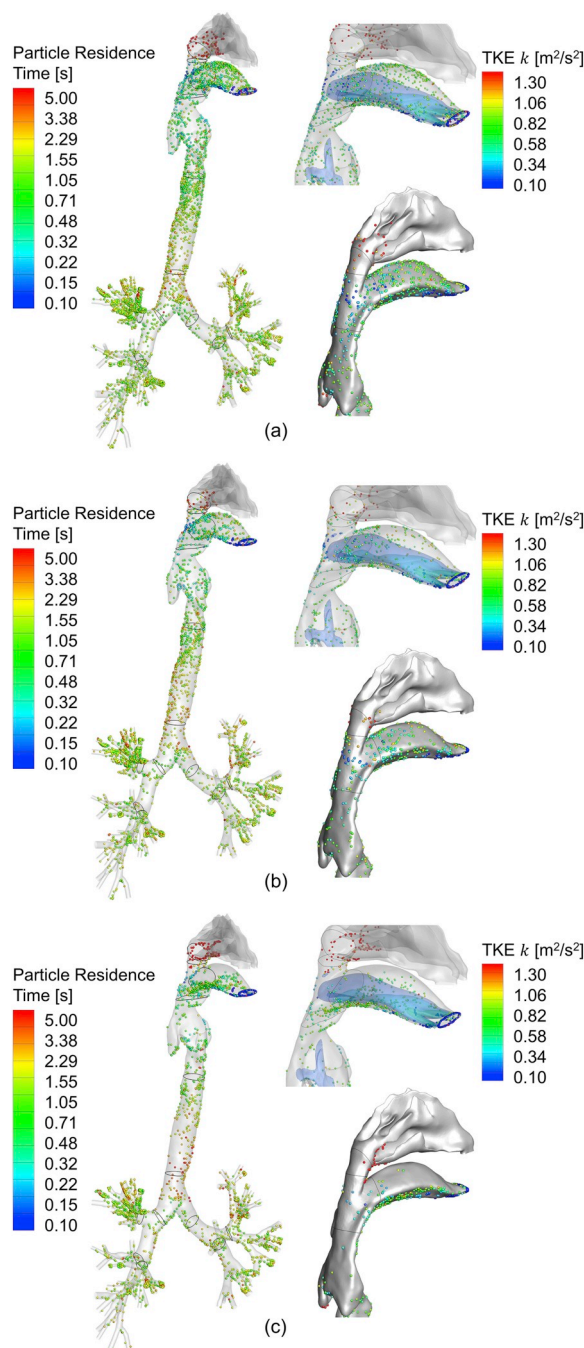


Fig. 8. Local airway deposition of metal fume particles with different diameters, accompanied by the iso-surfaces of airflow turbulence kinetic energy (TKE = 0.15, 0.30 and 0.60 m^2/s^2): (a) $d_p = 100$ nm, (b) $d_p = 190$ nm, and (c) $d_p = 830$ nm.

According to the particle residence time shown in Fig. 8, short particle residence time (approximately less than 0.5 s) indicates direct impaction as a consequence of the inertial effect. In contrast, deposited particles with a long residence time are driven by the secondary flow and Brownian motion. With the particle size increases, the inertial impaction will become dominant while the Brownian motion and secondary flow induced interception will become less significant. Compared with the regional depositions in the oropharynx, B1, and B2, higher $\text{RDF}_{\text{mouth}}$ s can be observed in the laryngopharynx and trachea because of the large airway wall surface areas ($8.5 \times 10^3 \text{ mm}^2$ and $7.3 \times 10^3 \text{ mm}^2$ for laryngopharynx and trachea, respectively, compared to $3.2 \times 10^3 \text{ mm}^2$ for oropharynx and $4.8 \times 10^3 \text{ mm}^2$ for B1) and stronger ambient turbulence waked by the laryngeal jet.

It is worth mentioning that the amount of particles entering each lobe is not proportional to the volumetric flow rate distributions. Among all the particles going into the main bronchi, approximately 55.0% can enter the right primary bronchus, whereas the total

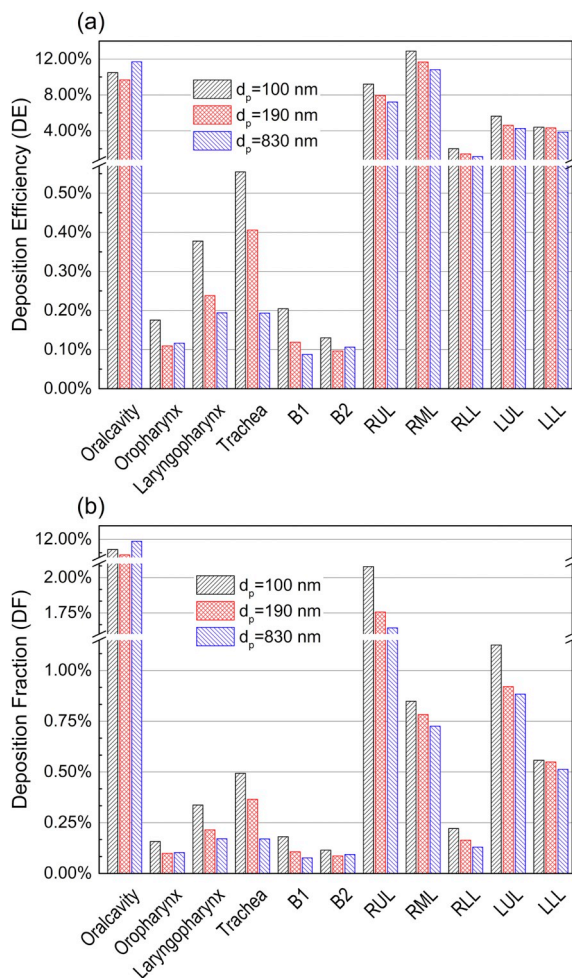


Fig. 9. Regional particle depositions in the human respiratory system: (a) regional deposition efficiencies (RDEs), and (b) regional deposition fractions (RDF_{mouth's}).

airflow rate percentage of the right lobes (RLs) is 52.2%. In addition, approximately 57% of particles transported into the two upper lobes (ULs) are carried by 47.2% of the total inspiratory airflow. Compared with the other four lobes, there are more particles that can enter the right upper lobe (RUL), in contrast with the relatively lower airflow rate percentage. Specifically, 30.5% of total particles that entered the main bronchi can reach the RUL, while the inspiratory flow rate via the RUL is only 21.66% of the total. The reason could be that as particles travel the shortest distance to reach the outlets through RUL, with the same particle tracking time, it allows a higher chance for particles hitting the wall in RUL. However, further studies are required to verify this speculation. The relatively low RDF in the right lower lobe (RLL) is because of reduced interception effect due to the lower secondary flows in the RLL. Since clinical research with statistical robustness also shows that ULs have higher lung cancer incidence rate than the other three lobes (Arame et al., 2014; Usuda et al., 2012), it is possible that high doses of inhaled microparticles could lead to higher health risks in ULs based on the higher deposition fractions we found in this study. However, more statistically robust investigations are needed to correlate the regional lung deposition with the cancer incidence rate in specific lung regions.

To evaluate the particle transport dynamics in human airways, RDEs (see Eq. (14)) are compared and shown in Fig. 9 (a). High RDEs can be observed in the oral cavity and five lobes. Specifically, the RDE in the oral cavity is higher than 9.6% due to the strong inertial impaction and interceptions induced by the recirculation flows. Moreover, RDEs are higher than 7.9% in the RUL and right middle lobe (RML) and over 3.9% in both LUL and left lower lobe (LLL), which indicates higher Brownian motion induced deposition in these regions. Also, the lower flow rate results in longer residence time and increases the chance of particle deposition. It is interesting to find that the RLL traps only about 1.1% of the entered particles, which is lower than the depositions in the other four lobes. Indeed, the airway path from the trachea to the RLL is relatively more straight compared with the other four lobes. Fig. 1 (c) shows the physiological differences of airways in different lobes. Accordingly, the flow is laminar, and the secondary flow induced by airway bending is the minimum in the RLL. Therefore, most particles entering the RLL can reach the outlets and escape without striking the airway walls with large curvatures.

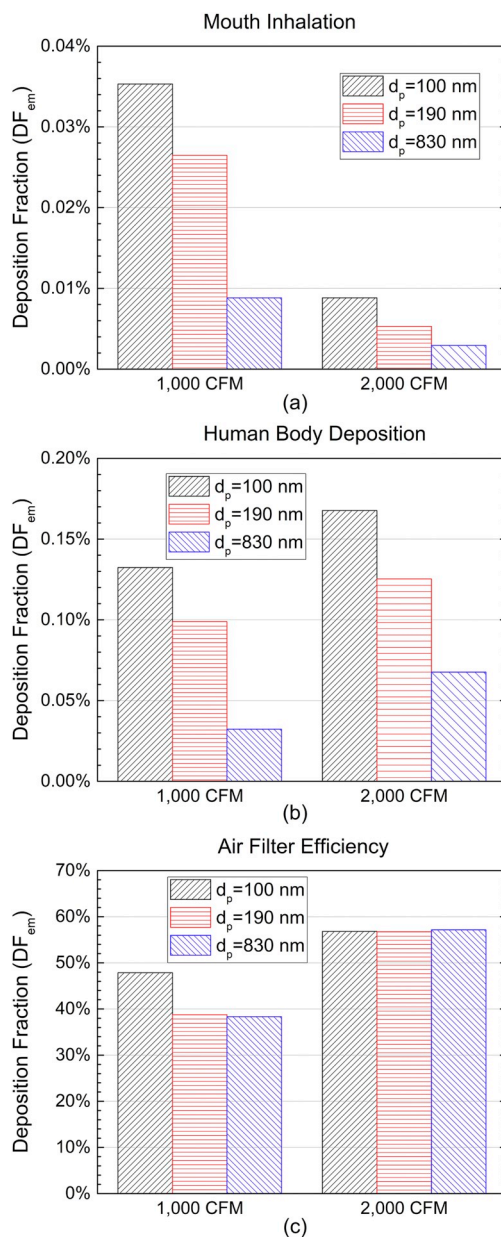


Fig. 10. Particle deposition and distributions at different air filter ventilation conditions: (a) $DF_{em}(\text{mouth})$, (b) $DF_{em}(\text{body})$, and (c) $DF_{em}(\text{air filters})$ in the virtual fabrication shop.

4.5. Ventilation effects on species transport

The ventilation effect on toxic gases filtration was also investigated and is shown in Fig. 5. As the ventilation rate decreases from 2,000 to 1,000 CFM, $j_{s,mouth}$ increases approximately by 215%. Specifically, $j_{s,mouth}$ was acquired by performing surface integration on the mouth inlet based on the simulation results shown in Figs. 5 (a) to (d). The airway absorption fractions of different gas species are quantitatively similar regardless of ventilation condition. Specifically, Fig. 5 compares \bar{Y}_s distribution in the respiratory tract at the sagittal plane ($y = -7.5$ mm) with two ventilation flow rates. Compared with high ventilation condition, the near-wall gradient of \bar{Y}_s is higher at low ventilation condition (shown in Fig. 5 (a) and (b)). The reason is that \bar{Y}_s is relatively high in airways at low ventilation condition. Therefore, to reach quasi-steady equilibrium at the airway wall (see the 3rd-type boundary condition shown in Eq. (7)), the near wall \bar{Y}_s gradient in the wall normal direction is also higher. The diffusion effect of gas species is stronger at low ventilation condition in the nasal cavity and nasopharynx, due to the higher concentration of inhaled gases. The higher concentration of inhaled gases is because of the higher gas concentration reaching the head region of the virtual human, which is due to the slower filtration at 1,000 CFM than 2,000 CFM.

Fig. 10 illustrates particle DF_{em} 's at the human mouth inlet, virtual body shell surface, and air filter inlets with the two ventilation conditions mentioned above. The inspiratory effects on particle transport can be observed in Fig. 10 (a), which shows that smaller particles have a higher probability of being inhaled via the mouth, especially at 1,000 CFM. It can also be observed that the inhaled particle number increases with the reduction of the filtration volumetric flow rate.

For particle deposition on the skin (shown in Fig. 10 (b)), smaller particles tend to have higher $DF_{em}(\text{body})$, because the particle loss due to the gravitational sedimentation is less and the residence times of suspended particles are longer due to the stronger Brownian motion for smaller particles. The combined effects increase the possibilities of smaller particles touching the virtual human body shell. Compared with the 2,000 CFM case, $DF_{em}(\text{body})$'s of 100, 190, and 830-nm particles decrease by 21.05%, 21.13%, and 52.17%, respectively, at 1,000 CFM. The comparison indicates that at higher ventilation volumetric flow rate, the induced longer particle suspension time increases the probability of particles hitting the walls of the virtual welding shop.

Furthermore, the filtration efficiency of the air filters is shown in Fig. 10 (c). An interesting observation is that at 2,000 CFM, the filtration efficiency is independent of particle size. It is because that the forced convection is dominant at 2,000 CFM and the difference of particle diffusion is negligible. However, the particle size effect on the filtration efficiency is noticeable at 1,000 CFM.

5. Conclusions

In this study, a CFPD based multiscale *in silico* model was developed. Specifically, by integrating the virtual working environment with a subject-specific human respiratory configuration, the model is able to provide noninvasive and cost-effective health risk assessments by predicting lung uptake and skin absorption of airborne welding fume particles and gases. Based on the numerical simulation results and the parametric analysis, quantitative conclusions are summarized as follows:

- (1) Above the welding emission source, the transport of selected gases is dominated by natural convection with the localized high temperature. When the local temperature is close to the room temperature, species transport is mainly affected by forced convection in the virtual welding fabrication room. \bar{Y}_s distribution in the subject-specific respiratory system is influenced by the local airflow velocity field and the corresponding $\bar{D}_{a-g,s}$. More than 90.0% of the inhaled NO and CO are absorbed in the human respiratory system with the inhalation flow rate equal to 11.87 L/min. In contrast, 51.2% and 62.2% of inhaled N₂O and NO₂ are absorbed, respectively. The airway wall absorption coefficient $\Gamma_{s,w}$ is the crucial factor that can impact pulmonary gas absorption.
- (2) The concentrated deposition patterns of larger particles are due to the dominant inertia impaction, while the more scattered deposition of smaller particles is because of the dominant diffusive behavior, i.e., the Brownian motion effect. Particles tend to enter the upper lobes more than other lobes regardless of the mass flow rate distribution in each lobe, which implies a higher vulnerability to have lung diseases in upper lobes. To confirm the causal relationships between the deposition patterns and the different lung cancer incidence rates in the five lobes, extensive investigations need to be done to draw statistically robust conclusions.
- (3) The ventilation condition is a key factor that can influence the inhaled gas absorption and particle deposition during the welding process. Specifically, the inhaled gas species mass flux is significantly higher at the poor ventilation condition, although the AF of the gases independent of the ventilation condition. Inadequate ventilations can induce an increase in the number of inhaled particles.

In summary, the representative virtual human and the CFPD model produce realistic and accurate lung aerosol dynamics to gain new physical insight and can provide high-resolution quantitative evidence to regulatory agencies for occupational exposure risk assessments. The model can be further extended for the health risk assessments on occupational exposures of other hazardous airborne aerosols, such as influenza A virus-laden droplets and respirable crystalline silica (RCS) (Bang et al., 2015; Kormuth et al., 2018).

6. Limitations of the study

Focusing on enhancing the fundamental understanding of welding fume and gas transport and deposition, simplifications of the CFPD based model in the present study include:

- (1) Adopting the particle number scale-up method between the welding fume emission source and the particle-entering mouth inlet (more details of the scale-up method are included in Appendix A: Supplementary Data);
- (2) Using the steady-state mouth inhalation pattern;
- (3) Employing the truncated respiratory system without small airways deeper than G6; and
- (4) Neglecting particle-particle interactions during their transport.

7. Future work

In light of the necessary simplifications made in the present numerical study, improvements are suggested as follows:

- (1) Evaluating fume source influence on the regional deposition and using realistic transient breathing waveforms for both mouth and nose respiration scenarios;

- (2) Employing a whole-lung model from mouth/nose to alveoli;
- (3) Predicting lung uptake and skin absorption for vulnerable sub-population groups with pre-existing lung diseases;
- (4) Considering particle-particle interactions and anisotropic particle shape effects; and
- (5) Integrating the PBTK model to extend the simulation capability and predict the uptakes of inhaled toxicants in different organs (Haghnegahdar et al., 2018).

Acknowledgments

This work was supported by the Southwest Center for Occupational and Environmental Health (SWCOEH) from National Institute for Occupational Safety and Health (NIOSH)/Centers for Disease Control and Prevention (CDC) under grant number 5T42OH008421 09. The use of ANSYS software (Canonsburg, PA) as part of the ANSYS-CBBL academic partnership agreement is gratefully acknowledged.

Appendix A. Supplementary Data

Supplementary data to this article can be found online at <https://doi.org/10.1016/j.jaerosci.2019.05.006>.

References

- Al-Ali, M. K., & Howarth, P. H. (1998). Nitric oxide and the respiratory system in health and disease. *Respiratory Medicine*, 92(5), 701–715. [https://doi.org/10.1016/S0954-6111\(98\)90000-2](https://doi.org/10.1016/S0954-6111(98)90000-2).
- Antonini, J. M., Taylor, M. D., Zimmer, A. T., & Roberts, J. R. (2004). Pulmonary responses to welding fumes: Role of metal constituents. *Journal of Toxicology and Environmental Health, Part A*, 67(3), 233–249. <https://doi.org/10.1080/15287390490266909>.
- Arame, A., Rivera, C., Foucault, C., Pricopi, C., Le Pimpec-Barthes, F., Mordant, P., et al. (2014). Is the lymphatic drainage of lung cancer lobe-specific? A surgical appraisal. *European Journal of Cardio-Thoracic Surgery*, 47(3), 543–549. <https://doi.org/10.1093/ejcts/ezu226>.
- Bang, K. M., Mazurek, J. M., Wood, J. M., White, G. E., Hendricks, S. A., Weston, A., et al. (2015). Silicosis mortality trends and new exposures to respirable crystalline silica - United States, 2001–2010. *MMWR (Morbidity and Mortality Weekly Report)*, 64(5), 117–120.
- Banko, A. J., Coletti, F., Schiavazzi, D., Elkins, C. J., & Eaton, J. K. (2015). Three-dimensional inspiratory flow in the upper and central human airways. *Experiments in Fluids*, 56(6), 117. <https://doi.org/10.1007/s00348-015-1966-y>.
- Bernate, J. A., Geisler, T. S., Padhy, S., Shaqfeh, E. S. G., & Iaccarino, G. (2017). Study of the flow unsteadiness in the human airway using large eddy simulation. *Physical Review Fluids*, 2(8), 083101. <https://doi.org/10.1103/PhysRevFluids.2.083101>.
- Brand, P., Bischof, K., Siry, L., Bertram, J., Schettgen, T., Reisgen, U., et al. (2013). Exposure of healthy subjects with emissions from a gas metal arc welding process: Part 3—biological effect markers and lung function. *International Archives of Occupational and Environmental Health*, 86(1), 39–45. <https://doi.org/10.1007/s00420-012-0740-1>.
- Calmet, H., Kleinstreuer, C., Houzeaux, G., Kolanjiyil, A., Lehmkühl, O., Olivares, E., et al. (2018). Subject-variability effects on micron particle deposition in human nasal cavities. *Journal of Aerosol Science*, 115, 12–28.
- Chen, X., Feng, Y., Zhong, W., & Kleinstreuer, C. (2017). Numerical investigation of the interaction, transport and deposition of multicomponent droplets in a simple mouth-throat model. *Journal of Aerosol Science*, 105, 108–127. <https://doi.org/10.1016/j.jaerosci.2016.12.001>.
- Chitano, P., Hosselet, J., Mapp, C., & Fabbri, L. (1995). Effect of oxidant air pollutants on the respiratory system: Insights from experimental animal research. *European Respiratory Journal*, 8, 1357–1371.
- Cui, X., & Gutheil, E. (2017). Three-dimensional unsteady large eddy simulation of the vortex structures and the mono-disperse particle dispersion in the idealized human upper respiratory system. *Journal of Aerosol Science*, 114, 195–208.
- Daigle, C. C., Chalupa, D. C., Gibb, F. R., Morrow, P. E., Oberdörster, G., Utell, M. J., et al. (2003). Ultrafine particle deposition in humans during rest and exercise. *Inhalation Toxicology*, 15(6), 539–552. <https://doi.org/10.1080/08958370304468>.
- De Flora, S. (2000). Threshold mechanisms and site specificity in chromium (VI) carcinogenesis. *Carcinogenesis*, 21(4), 533–541. <https://doi.org/10.1093/carcin/21.4.533>.
- Dong, J., Ma, J., Shang, Y., Inthavong, K., Qiu, D., Tu, J., et al. (2018). Detailed nanoparticle exposure analysis among human nasal cavities with distinct vestibule phenotypes. *Journal of Aerosol Science*, 121, 54–65. <https://doi.org/10.1016/j.jaerosci.2018.05.001>.
- Feng, & Kleinstreuer, C. (2013). *Analysis of non-spherical particle transport in complex internal shear flows, Vol 25*.
- Feng, Y., & Kleinstreuer, C. (2013). Analysis of non-spherical particle transport in complex internal shear flows. *Physics of Fluids*, 25(9), 091904.
- Feng, & Kleinstreuer, C. (2014). Micron-particle transport, interactions and deposition in triple lung-airway bifurcations using a novel modeling approach. *Journal of Aerosol Science*, 71, 1–15. <https://doi.org/10.1016/j.jaerosci.2014.01.003>.
- Feng, Kleinstreuer, C., Castro, N., & Rostami, A. (2016). Computational transport, phase change and deposition analysis of inhaled multicomponent droplet–vapor mixtures in an idealized human upper lung model. *Journal of Aerosol Science*, 96, 96–123. <https://doi.org/10.1016/j.jaerosci.2016.03.001>.
- Feng, Kleinstreuer, C., & Rostami, A. (2015). Evaporation and condensation of multicomponent electronic cigarette droplets and conventional cigarette smoke particles in an idealized G3–G6 triple bifurcating unit. *Journal of Aerosol Science*, 80, 58–74. <https://doi.org/10.1016/j.jaerosci.2014.11.002>.
- Feng, Zhao, J., Chen, X., & Lin, J. (2017). An in silico subject-variability study of upper airway morphological influence on the airflow regime in a tracheobronchial tree. *Bioengineering*, 4(4), 90.
- Feng, Zhao, J., Kleinstreuer, C., Wang, Q., Wang, J., Wu, D. H., et al. (2018). An in silico inter-subject variability study of extra-thoracic morphology effects on inhaled particle transport and deposition. *Journal of Aerosol Science*, 123, 185–207. <https://doi.org/10.1016/j.jaerosci.2018.05.010>.
- Golbabaei, F., & Khadem, M. (2015). *Air pollution in welding processes - assessment and control methods*.
- Goldak, J., Chakravarti, A., & Bibby, M. (1984). A new finite element model for welding heat sources. *Metallurgical Transactions B*, 15(2), 299–305. <https://doi.org/10.1007/BF02667333>.
- Gosman, A. D., & Ioannides, E. (1983). *Aspects of computer simulation of liquid-fueled combustor, Vol 7*.
- Graczyk, H., Lewinski, N., Zhao, J., Sauvain, J.-J., Suarez, G., Wild, P., et al. (2016). Increase in oxidative stress levels following welding fume inhalation: A controlled human exposure study. *Particle and Fibre Toxicology*, 13(1), 31. <https://doi.org/10.1186/s12989-016-0143-7>.
- Gupta, J. K., Lin, C.-H., & Chen, Q. (2012). Risk assessment of airborne infectious diseases in aircraft cabins. *Indoor Air*, 22(5), 388–395. <https://doi.org/10.1111/j.1600-0668.2012.00773.x>.
- Haghnegahdar, A., Feng, Y., Chen, X., Lin, J. J. A. S., & Technology (2018). Computational analysis of deposition and translocation of inhaled nicotine and acrolein in the human body with e-cigarette puffing topographies. 52(5), 483–493.
- Haghnegahdar, A., Zhao, J., & Feng, Y. (2019). Lung aerosol dynamics of airborne influenza A virus-laden droplets and the resultant immune system responses: An in silico study. *Journal of Aerosol Science*, 134, 21.
- Hannu, T., Piipari, R., Tuppurainen, M., Nordman, H., & Tuomi, T. (2007). Occupational asthma caused by stainless steel welding fumes: A clinical study. *European Respiratory Journal*, 29(1), 85–90. <https://doi.org/10.1183/09031936.00058106>.
- Heyder, J. (2004). Deposition of inhaled particles in the human respiratory tract and consequences for regional targeting in respiratory drug delivery. *Proceedings of the American Thoracic Society*, 1(4), 315–320. <https://doi.org/10.1513/pats.200409-046TA>.

- Horstman, D. H., Ball, B. A., Brown, J., Gerrity, T., & Folinsbee, L. J. (1995). Comparison of pulmonary responses of asthmatic and nonasthmatic subjects performing light exercise while exposed to a low level of ozone. *Toxicology and Industrial Health*, 11(4), 369–385. <https://doi.org/10.1177/074823379501100401>.
- Hou, R., Evans, D. M., McClure, J., Nunes, A. C., & Garcia, G. (1996). *Shielding gas and heat transfer efficiency in plasma arc welding: Shielding gas flow rate is shown to have an appreciable effect on the size of the weld and the HAZ, Vol 75*.
- Kampa, M., & Castanas, E. (2008). Human health effects of air pollution. *Environmental Pollution*, 151(2), 362–367. <https://doi.org/10.1016/j.envpol.2007.06.012>.
- Khadem, M., Golbabaee, F., Hosseini, M., Hassani, H., Ghahri, A., Divani, R., et al. (2012). *Exposure to metal fumes among confined spaces welders, Vol 3*.
- Kim, J. Y., Chen, J.-C., Boyce, P. D., & Christiani, D. C. (2005). Exposure to welding fumes is associated with acute systemic inflammatory responses. *Occupational and Environmental Medicine*, 62, 157–163.
- Kim, Y., Tong, Z., Chan, H., & Yang, R. (2019). CFD modelling of air and particle flows in different airway models. *Journal of Aerosol Science*, 134, 14–28.
- Kleinstreuer, C. (1997). *Analyses of basic fluid flow problems Engineering fluid dynamics: An interdisciplinary systems approach*. Cambridge: Cambridge University Press 113–252.
- Kolanjyil, A. V., & Kleinstreuer, C. (2017). Computational analysis of aerosol-dynamics in a human whole-lung airway model. *Journal of Aerosol Science*, 114, 301–316.
- Kormuth, K. A., Lin, K., Prussin, A. J., 2nd, Vejerano, E. P., Tiwari, A. J., Cox, S. S., et al. (2018). Influenza virus infectivity is retained in aerosols and droplets independent of relative humidity. *The Journal of Infectious Diseases*, 218(5), 739–747. <https://doi.org/10.1093/infdis/jiy221>.
- Koullapis, P., Nicolaou, L., & Kassinou, S. C. (2018). In silico assessment of mouth-throat effects on regional deposition in the upper tracheobronchial airways. *Journal of Aerosol Science*, 117, 164–188.
- Koullapis, P. G., Nicolaou, L., & Kassinou, S. C. (2018). In silico assessment of mouth-throat effects on regional deposition in the upper tracheobronchial airways. *Journal of Aerosol Science*, 117, 164–188. <https://doi.org/10.1016/j.jaerosci.2017.12.001>.
- Lambert, A. R., O'Shaughnessy, P., Tawhai, M. H., Hoffman, E. A., & Lin, C.-L. (2011). Regional deposition of particles in an image-based airway model: Large-eddy simulation and left-right lung ventilation asymmetry. *Aerosol Science & Technology*, 45(1), 11–25. <https://doi.org/10.1080/02786826.2010.517578>.
- Li, A., & Ahmadi, G. (1993). Deposition of aerosols on surfaces in a turbulent channel flow. *International Journal of Engineering Science*, 31(3), 435–451. [https://doi.org/10.1016/0020-7225\(93\)90017-0](https://doi.org/10.1016/0020-7225(93)90017-0).
- Lin, C.-L., Tawhai, M. H., McLennan, G., & Hoffman, E. A. (2007). Characteristics of the turbulent laryngeal jet and its effect on airflow in the human intra-thoracic airways. *Respiratory Physiology and Neurobiology*, 157(2–3), 295–309. <https://doi.org/10.1016/j.resp.2007.02.006>.
- Longest, P. W., Bass, K., Dutta, R., Rani, V., Thomas, M. L., El-Achwah, A., et al. (2019). Use of computational fluid dynamics deposition modeling in respiratory drug delivery. *Expert Opinion on Drug Delivery*, 16(1), 7–26. <https://doi.org/10.1080/17425247.2019.1551875>.
- Mansour, H., & Rhee Xiao Wu, Y.-S. (2009). *Nanomedicine in pulmonary delivery, Vol 4*.
- Massman, W. J. (1998). A review of the molecular diffusivities of H₂O, CO₂, CH₄, CO, O₃, SO₂, NH₃, N₂O, NO, and NO₂ in air, O₂ and N₂ near STP. *Atmospheric Environment*, 32(6), 1111–1127. [https://doi.org/10.1016/S1352-2310\(97\)00391-9](https://doi.org/10.1016/S1352-2310(97)00391-9).
- Menter, F. R. (1994). Two-equation eddy-viscosity turbulence models for engineering applications. *AIAA Journal*, 32(8), 1598–1605.
- Menter, Langtry, R., & Völker, S. (2006). Transition modelling for general purpose CFD codes. *Flow, Turbulence and Combustion*, 77(1), 277–303. <https://doi.org/10.1007/s10494-006-9047-1>.
- Nicolaou, L. (2018). Inertial and gravitational effects on aerosol deposition in the conducting airways. *Journal of Aerosol Science*, 120, 32–51.
- NIOSH (2019). *Welding fumes*. Retrieved from <https://www.cdc.gov/niosh/pe/88/welding.html>.
- Pires, I., Quintino, L., Amaral, V., & Rosado, T. (2010). Reduction of fume and gas emissions using innovative gas metal arc welding variants. *International Journal of Advanced Manufacturing Technology*, 50(5–8), 557–567.
- Poudyal, I., & Adhikari, N. P. (2014). Temperature dependence of diffusion coefficient of carbon monoxide in water: A molecular dynamics study. *Journal of Molecular Liquids*, 194, 77–84. <https://doi.org/10.1016/j.molliq.2014.01.004>.
- Saffman, P. G. (1965). The lift on a small sphere in a slow shear flow. *Journal of Fluid Mechanics*, 22(2), 385–400. <https://doi.org/10.1017/S0022112065000824>.
- Sander, R. (2015). Compilation of Henry's law constants (version 4.0) for water as solvent. *Atmospheric Chemistry and Physics*, 15(8), 4399–4981. <https://doi.org/10.5194/acp-15-4399-2015>.
- Scheel, L. D., Dobrogorski, O. J., Mountain, J. T., Svirbely, J. L., & Stokinger, H. E. (1959). Physiologic, biochemical, immunologic and pathologic changes following ozone exposure. *Journal of Applied Physiology*, 14(1), 67–80. <https://doi.org/10.1152/jappl.1959.14.1.67>.
- Sjögren, B., Hansen, K. S., Kjuus, H., & Persson, P. G. (1994). Exposure to stainless steel welding fumes and lung cancer: A meta-analysis. *Occupational and Environmental Medicine*, 51(5), 335–336. <https://doi.org/10.1136/oem.51.5.335>.
- Spengler, J. D., & Chen, Q. (2000). Indoor air quality factors in designing a healthy building. *Annual Review of Energy and the Environment*, 25(1), 567–600. <https://doi.org/10.1146/annurev.energy.25.1.567>.
- Sul, B., Oppito, Z., Jayasekera, S., Vanger, B., Zeller, A., Morris, M., ... Day, S. (2018). Assessing airflow sensitivity to healthy and diseased lung conditions in a computational fluid dynamics model validated in vitro. *Journal of Biomechanical Engineering*, 140(5), 051009.
- Tamimi, A., B. Rinker, E., & Sandall, O. (1994). *Diffusion coefficients for hydrogen sulfide, carbon dioxide, and nitrous oxide in water over the temperature range, Vol 39*, 293–368.
- Tian, G., Hindle, M., Lee, S., & Longest, P. W. (2015). Validating CFD predictions of pharmaceutical aerosol deposition with in vivo data. *Pharmaceutical Research*, 32(10), 3170–3187. <https://doi.org/10.1007/s11095-015-1695-1>.
- Usuda, J., Kajiwara, N., Ikeda, N., Ohira, T., Shimada, Y., Kudo, Y., ... Nomura, M. (2012). Do tumours located in the left lower lobe have worse outcomes in lymph node-positive non-small cell lung cancer than tumours in other lobes? *European Journal of Cardio-Thoracic Surgery*, 42(3), 414–419. <https://doi.org/10.1093/ejcts/ezs065>.
- Utzinger, J. (2004). Health impact assessment: Concepts, theory, techniques, and applications. *Bulletin of the World Health Organization*, 82(12) 954–954.
- Wang, J., Hoang, T., Floyd, E. L., & Regens, J. L. (2017b). Characterization of particulate fume and oxides emission from stainless steel plasma cutting. *Annals of Work Exposures and Health*, 61(3), 311–320. <https://doi.org/10.1093/annweh/wxw031>.
- WAT (2019). *MIG shielding gas flow rate chart*. Retrieved from http://www.netwelding.com/MIG_Flow%20Rate-Chart.htm.
- Wilcox, D. C. (2006). *Turbulence Modeling for CFD: DCW industries, Inc*.
- Xi, J., Yuan, J. E., Yang, M., Si, X., Zhou, Y., & Cheng, Y.-S. (2016). Parametric study on mouth-throat geometrical factors on deposition of orally inhaled aerosols. *Journal of Aerosol Science*, 99, 94–106. <https://doi.org/10.1016/j.jaerosci.2016.01.014>.
- Xu, X., Shang, Y., Tian, L., Weng, W., & Tu, J. (2018). A numerical study on firefighter nasal airway dosimetry of smoke particles from a realistic composite deck fire. *Journal of Aerosol Science*, 123, 91–104.
- Yoo, S.-J., & Ito, K. (2018). Assessment of transient inhalation exposure using in silico human model integrated with PBPK-CFD hybrid analysis. *Sustainable Cities and Society*, 40, 317–325. <https://doi.org/10.1016/j.scs.2018.04.023>.
- Zacharia, I. G., & Deen, W. M. (2005). Diffusivity and solubility of nitric oxide in water and saline. *Annals of Biomedical Engineering*, 33(2), 214–222. <https://doi.org/10.1007/s10439-005-8980-9>.
- Zhang, M., Jian, L., Bin, P., Xing, M., Lou, J., Cong, L., et al. (2013). Workplace exposure to nanoparticles from gas metal arc welding process. *Journal of Nanoparticle Research*, 15(11), 2016.
- Zhang, Z., & Kleinstreuer, C. (2011). Laminar-to-turbulent fluid-nanoparticle dynamics simulations: Model comparisons and nanoparticle-deposition applications. *International Journal for Numerical Methods in Biomedical Engineering*, 27(12), 1930–1950. <https://doi.org/10.1002/cnm.1447>.
- Zhang, Z., Kleinstreuer, C., & Feng, Y. (2012a). Vapor deposition during cigarette smoke inhalation in a subject-specific human airway model. *Journal of Aerosol Science*, 53, 40–60.
- Zhang, Z., Kleinstreuer, C., & Hyun, S. (2012b). Size-change and deposition of conventional and composite cigarette smoke particles during inhalation in a subject-specific airway model. *Journal of Aerosol Science*, 46, 34–52. <https://doi.org/10.1016/j.jaerosci.2011.12.002>.